Liquid film and heat transfer characteristics during superheated wall cooling via pulsed injection of a liquid jet

Noritaka Sako[1*], Kouhei Noda[1], Jun Hayashi[1], Yu Daimon[2] and Hiroshi Kawanabe[1]

[1] Department of Energy Science, Kyoto University, Yoshida Honmachi, Sakyo-ku, Kyoto 606-8501, Japan

Email: sako.noritaka.32c@st.kyoto-u.ac.jp

[2] Research Unit III, Research and Development Directorate, Japan Aerospace Exploration Agency, 2-1-1 Sengen, Tsukuba, Ibaraki 305-8505, Japan

Abstract

Pulse firing is one of the major operation modes of bipropellant thrusters for the attitude control of small-scale spacecrafts. In the pulse-firing mode, the operational range of the thruster depends on the deterioration of liquid film cooling performance. Because cooling performance is determined by the balance of heat removed by the liquid film and transferred to the manifold, the behavior and heat transfer characteristics of liquid films under the intermittent injection of liquid jets must be understood to enable a wider range of operational patterns. We conducted cooling tests on a superheated metal plate via the pulsed injection of a liquid jet for better understanding of the pulsed cooling process. Different injection patterns, including continuous injection, with the same injection quantity were examined on two types of metal plates (aluminum alloy and copper), because the thermal properties of metal plates affect both the heat transfer characteristics of the liquid film and temperature rise of the plate during the inter-pulse duration. The cooling process was evaluated based on the evolution of the liquid film on the metal plate and rear-side temperature of the metal plate. The evolution and temperature were simultaneously visualized using a high-speed camera and infrared camera, respectively. To link the liquid film state to the heat transfer process, the temperature and heat flux on the cooled surface were estimated by solving the inverse problem of three-dimensional transient heat conduction. The results indicate that the wetting front position corresponds to the position of the maximum temperature gradient. Additionally, the residual liquid film is consumed through the

evaporation and the droplet dispersion related to the nucleate boiling. The effects of thermal inertia and diffusivity of the metal plate highlight the differences in the amount of heat removed by the liquid film. The heat removed by the liquid film during pulsed cooling exhibited a peak and was higher than that removed by continuous injection on the aluminum alloy plate. Less heat was removed under low-duty-cycle conditions, and the amount of heat removed by the liquid film was lower than that removed by continuous injection on the copper plate.

Keywords: jet impingement, quenching, pulsed injection, liquid film, heat transfer

Nomenclature

A_{wet}	wetted area [m^2]
c_{w}	specific heat of test plate [J kg^{-1} K^{-1}]
d	inner diameter of nozzle [m]
DC	duty cycle [%]
f_{p}	pulse frequency [Hz]
g	gravitational acceleration [m s^{-2}]
h_{lv}	latent heat of the test liquid [J kg^{-1}]
k_{w}	thermal conductivity of test plate [W m^{-1} K^{-1}]
k_{v}	thermal conductivity of vapor [W m^{-1} K^{-1}]
N	pulse number [-]
P_{v}	force per unit area by vapor flow [Pa]
q_{s}	surface heat flux [W m^{-2}]
q_{th}	threshold value for the calculation of Eq. (5) [W m^{-2}]
$\dot{Q}$	rate of heat transfer from metal plate to liquid film [W]
Q^*	nondimensional removed heat defined by Eq. (8) [-]
$Q_{N_{\mathrm{th}}}$	amount of heat removed by liquid film during the N_{th} period [J]

Q_t	total amount of heat removed by liquid film [J]
Re_j	jet Reynolds number ($=\frac{u_\mathrm{j}d}{\nu_\mathrm{l}}$) [-]
t	elapsed time after the start of a cooling test [s]
T_w	temperature of test plate [K]
T_wf	temperature at the wetting front [K]
T_cr	critical temperature [K]
ΔT_min	minimum value of temperature difference defined by Eq. (7) [K]
ΔT_sup	degree of wall superheating [K]
u_j	jet velocity at nozzle exit [m s^{-1}]
u_v	velocity of vapor flow [m s^{-1}]
x_g	position where spatial temperature gradient is maximized [m]
x_wf	position of the wetting front relative to the impingement point [m]
x, y, and z	coordinates of impingement point of liquid jet [m]
α_w	thermal diffusivity of test plate [m^2 s^{-1}]
δ	thickness of wall [m]
θ	impingement angle [°]
μ_v	viscosity of vapor [Pa s]
ν_l	kinematic viscosity of test liquid [m^2 s^{-1}]
ρ_l	density of test liquid [kg m^{-3}]
ρ_v	density of vapor [kg m^{-3}]
ρ_w	density of test plate [kg m^{-3}]
σ	surface tension [N m]
τ_p	pulse period [s]

1. Introduction

Liquid jet impingement cooling, which forms a liquid film, is widely used in applications requiring high heat dissipation, including material processes [1–3] and the cooling of nuclear reactor cores [4, 5], for its high cooling ability. This ability is attributed to the latent heat transfer through phase change from liquid to vapor. Liquid jet impingement on a solid wall also occurs in bipropellant thrusters, which are applied for the attitude control and orbit maneuvering of small-scale spacecraft and satellites [6–8]. Liquid jets of fuel are impinged on the chamber wall to protect it from high-temperature combustion gases. This cooling process is called film cooling [6]. Figure 1 illustrates a schematic of film cooling inside the combustion chamber of the thrusters. These thrusters generally employ hypergolic propellants, which are typically a combination of nitrogen tetroxide / hydrazine-derivative fuel [9]. These propellants react immediately upon contact with each other without requiring ignition devices [10]. Based on the fast response of the chemical reaction of these propellants, the propulsion system is operated in the pulse-firing mode, with firing times ranging from $O(10)$ ms to $O(10^2)$ ms [10, 11]. During the combustion event, the maximum thermal load appears around the nozzle throat, and a large temperature gradient is formed from the throat to the impingement point [12]. The heat stored around the throat is transferred toward the side of the injector faceplate by heat conduction inside the chamber wall when the supply of propellants is stopped, which is called heat soak-back [13]. Therefore, the situation that the fuel jets for film cooling are injected onto the hot surface formed by heat soak-back can be appeared depending on the conditions of the interval between each pulsed-combustion event. An illustration summarizing the events described above was provided in our previous study [14]. In other words, the combustion chamber wall may not be cooled sufficiently if the pulse interval and associated heat soak-back conditions are unfavorable. The operational range of the pulse-firing mode is determined by cooling performance requirements (i.e., heat resistance of the thrusters). For better thermal management and a wider operational range of thrusters, the cooling processes of hot surfaces under liquid jet impingement must be understood.

When a liquid jet is impinged onto a surface with a temperature exceeding the Leidenfrost point, the formed liquid film is deflected from the surface at the leading edge because of vigorous boiling.

The leading edge, which is the boundary between the wetted and dry regions, is called the wetting front. Different cooling modes (single-phase forced convection, nucleate boiling, and transition boiling) coexist in the wetted region [15, 16]. For well-controlled cooling processes, many studies have been dedicated to understanding the processes of wetting front propagation and heat transfer characteristics inside the wetted region [1–5, 14–20]. However, the physical phenomena of wetting front behavior during quenching have not yet been elucidated [21, 22]. Recently, we conducted an experiment and discovered that the wetting front propagation and maximum heat flux achieved near the wetting front were affected by the liquid flow rate, rather than the liquid jet velocity [14].

Although heat transfer characteristics during continuous liquid jet injection have been extensively investigated, the cooling process with intermittently injected liquid jets, which is found in the pulse-firing mode of bipropellant thrusters, is not well understood. Recently, Wessenberg et al. [23] investigated the heat transfer efficiency of the pulsed injection of water jets during the single-phase convection cooling mode. Abishek and Narayanaswamy [24] investigated the effects of pulsed injection on boiling heat transfer characteristics, including the heat flux in the nucleate boiling region and critical heat flux, using water and FC72 as coolants. However, the effects of pulsed injection of a liquid jet on the heat transfer characteristics have not been thoroughly investigated [23], and few studies have investigated two-phase cooling via pulsed injection of liquid jets [25].

Moreover, few studies have examined the transient formation processes of a liquid film during the pulse-firing mode in real bipropellant thrusters. For the first time, Fujii et al. [6] succeeded in optically capturing unsteady liquid film dynamics during the operation of the pulse-firing mode using a quartz glass chamber and confirmed that the liquid film length in a glass chamber was longer than that in an actual combustion chamber because of reduced heat input from the chamber wall. To recognize the differences in liquid film behavior on both types of chamber walls, the unsteady dynamics of a liquid film on an actual chamber wall must also be investigated. However, direct optical observation of the physical phenomena inside the chamber walls of bipropellant thrusters is infeasible because they are generally made of niobium alloy [26], ceramic [27], or precious metals [28]. A method that captures the liquid film behavior inside the chamber by measuring only the temperature distribution on the outer surface of the chamber wall will be beneficial for a better understanding of it. The liquid film length in the steady state in an actual chamber can be derived from the temperature distribution on the outer surface of the chamber measured by an infrared camera [29]. An infrared imaging method with high spatial resolution has the potential to provide valuable information regarding the heat transfer characteristics between the liquid film and the chamber wall [30].

In this study, we conducted transient cooling tests on hot metal plate surfaces under pulsed injection of a liquid jet to gain insights into liquid film behavior during pulsed cooling. Although several factors dominate the liquid film behavior in the actual thruster, such as turbulent heat transfer from the combustion gases and hydrodynamic instabilities at the gas–liquid interface (Fig. 1), this study focuses on the heat transfer between the liquid film and the wall. Initially, we focus on understanding the liquid film behavior during the pulsed cooling based on both visualization images and the measured temperature of the metal plate. Because we proved the temperature measured on the opposite side of a cooled surface to represent the cooling process in our previous study [14], we applied this measurement technique to analyze the liquid film behavior during pulsed cooling. Next, we concentrate on the improvement of the cooling performance by pulsed injection. In the operation of the current thrusters, the injection of liquid fuel for film cooling is synchronized with that of the propellant for combustion (main injection). The cooling performance is considered to be governed by the balance between the amount of cooling during injection and temperature rise of the metal plate during the period between injections. Therefore, the cooling performance could be improved by pulsed injection controlled independently to the main injection considering the heat soak-back phenomenon. Thus, pulsed cooling tests with the same amount of liquid but different flow rates and duty cycles (DCs = ratio of injection duration over one period) were examined for the improvement of the cooling performance. A continuous cooling test with the time-averaged flow rate of the pulsed cooling tests was also conducted for the control condition. Additionally, the thermal properties of the metal plate affect its temperature rise, which eventually influences the heat transfer characteristics of the liquid film. Therefore, in this study, two different metal plates were considered to evaluate the effects of their thermal properties (i.e., thermal diffusivity or thermal inertia).

The remainder of this paper is organized as follows. Section 2 describes the experimental design adopted in this study. Section 3 presents and discusses the experimental results. Section 4 summarizes the findings and concludes the study.

2. Experimental design

2.1 Experimental setup

Figure 2 presents a schematic of the experimental setup for the simultaneous measurement of liquid film behavior and temperature distributions. The coordinate system for the experiments is defined in Fig. 2. The origin was defined as the impingement point of the liquid jet. A liquid jet was intermittently injected from a liquid tank pressurized with compressed air. The opening and closing times were controlled by a solenoid valve operated by signals from a function generator (NF Corporation, WF1948). A rod heater was inserted downstream of the metal plate to heat the plate. A rod heater was utilized to simulate the scenario in which the liquid film flows against the direction of the heat input (i.e., from downstream to upstream) as is the heat flow direction inside the chamber wall of the bipropellant thrusters. In this study, liquid film behavior was primarily observed from the side using the backlight technique with a high-speed camera (Photron FAST-CAM SA-1.1) to capture the wetting front position clearly. Additionally, high-speed imaging was performed from the front (cooled) side, as described in our previous study [14]. The frame rate and exposure time were 500 fps and 20 μs, respectively. The spatial resolutions for the side and front views were 0.16 and 0.09 mm/pixel, respectively. The temperature distribution on the rear surface of the metal plate was measured using an infrared camera (NIPPON AVIONICS InfReC R550Pro). The frame rate and spatial resolution for temperature measurement were 60 fps and 0.22 mm/pixel, respectively. The rear-side of the metal plate was painted with blackbody spray to ensure an emissivity of 0.94. The measurement accuracy of the infrared camera used in this study was ±2 ℃. To investigate the effects of thermal properties of the metal plate on pulsed cooling, an aluminum alloy (A5052) and copper (C1100) were employed as test plate materials with a thickness of 3 mm, width of 50 mm, and length of 80 mm. The temperature measurement area was restricted to a length of 70 mm and width of 46 mm. In this study, oxidization of the metal surface could not be avoided, and the oxide layer on the surface affected the cooling process [31]. Therefore, the metal surface was fully oxidized via heating, and then cooling tests were conducted several times before data acquisition to ensure stable surface properties and reproducibility.

Water was employed as a test liquid because its density and surface tension resemble those of hydrazine. The nozzle diameter d (i.e., liquid jet diameter) and impingement angle θ (Fig. 2) were fixed at 1.1 mm and 10°, respectively. The ratio of the distance between the nozzle outlet and test plate (i.e., liquid jet length) to the nozzle diameter L/d was set to six. The test liquid (approximately 20 °C) was injected onto the test plate when the temperature of the impingement point increased to 220 °C. The temperatures of the rod heater were set to 600 and 500 °C in the cases of the aluminum alloy and copper plates, respectively, to raise the temperature of the impingement point to 220 °C while forming a stable initial temperature distribution. The initial temperature distribution along the x axis is presented in Fig. 3. For the pulsed injection conditions, the pulse frequency f_{p} was set to 1.0 Hz, which corresponded to a pulse period of τ_{p} $(=1/f_{\mathrm{p}})$ = 1.0 s. The number of pulses was fixed to three. The flow rate of the test liquid and DC were varied, while the total injection quantity of the test liquid was kept constant during each pulse period. Additionally, a continuous injection test with the time-averaged flow rate of the pulsed cooling tests was conducted to compare the total amount of heat removed by the liquid film in the pulsed and continuous cooling tests. The pulsed injection conditions are listed in Table 1. For each condition, the cooling tests were conducted five times.

The temperature and heat flux on the front (cooled) surface must be estimated to evaluate the heat transfer characteristics between the liquid film and the metal surface. For this estimation, the inverse heat conduction problem was numerically solved using the measured temperature distribution on the rear surface. The transient heat conduction equation for the metal plate based on Cartesian coordinates is given as follows:

$$\rho_{\mathrm{w}} c_{\mathrm{w}} \frac{\partial T_{\mathrm{w}}}{\partial t} = k_{\mathrm{w}} \left(\frac{\partial^2 T_{\mathrm{w}}}{\partial x^2} + \frac{\partial^2 T_{\mathrm{w}}}{\partial y^2} + \frac{\partial^2 T_{\mathrm{w}}}{\partial z^2} \right) \tag{1}$$

To solve Eq. (1), the fully implicit scheme and finite volume method were employed for time integration and spatial discretization, respectively. The time step was 1/60 s, which was determined based on the frame rate used for temperature measurement. A rectangular computation domain with a width of 46 mm, length of 70 mm (measurement area), and thickness of 3 mm was divided into 69 × 105 × 3 cells. The initial and boundary conditions were the same as those used in our previous study [14]. The temperature dependence of the thermal properties was not considered in this study (aluminum alloy: ρ_{w} = 2680 kg/m^3, c_{w} = 900 J/kg · K, k_{w} = 137 W/m · K; copper: ρ_{w} = 8900 kg/m^3, c_{w} = 385 J/kg · K, k_{w} = 391 W/m · K). Detailed information regarding the inverse heat conduction problem and data reduction was provided in our previous paper [14].

3. Results and discussion

This section first provides an overview of the liquid film behavior and heat transfer characteristics between the liquid film and the metal surface in the pulsed cooling tests. Next, the liquid film behaviors and the amount of heat removed by the liquid film in the pulsed and continuous cooling tests are compared. Each injection and non-injection periods were defined as the "N^{th} ON time" and "N^{th} OFF time," respectively. For example, the 1$^{\text{st}}$ ON time and 1$^{\text{st}}$ OFF time under the condition of f_{p} = 1.0 Hz and 50% DC correspond to the periods of t = 0–0.5 and 0.5–1.0 s, respectively, with allowances for the open and close response times of the solenoid valve. Additionally, the "N^{th} period" indicates the period of $t = (N-1) \cdot \tau_{\mathrm{p}}$ s– $N \cdot \tau_{\mathrm{p}}$ s.

3.1 Liquid film behavior and heat transfer characteristics during pulsed cooling

In this section, the results for the aluminum alloy under the condition of 50% DC are used as representative data to explain the liquid film behavior and heat transfer characteristics during pulsed cooling. Figure 4 presents an image of a liquid film captured from the front and the distributions of the estimated temperature and heat flux on the front surface at an elapsed time of 0.5 s, which corresponds to the end of injection for the 1st ON time. During the 1st ON time, the wetting front gradually propagates downstream from the start of the injection and eventually reaches the position highlighted in Fig. 4. In this study, the distance from the impingement point to the wetting front along the x axis was defined as x_{wf}, as displayed in Fig. 4. The maximum heat flux can be observed in the wetted area near the wetting front [14, 15], and a relatively higher heat flux can be observed in the region near the impingement point. These trends in the results during the 1st ON time were the same as those observed in our previous study for the continuous cooling test [14].

Figure 5 presents a time series of visualization images, and the estimated temperature and heat flux on the front surface during the 1st OFF time. Notably, the contour range for the heat flux is different from that in Fig. 4. As illustrated in Fig. 5, the residual liquid film is consumed by nucleate boiling through the evaporation and ejection of droplets as the bubbles are ruptured [32]. Nucleate boiling of the residual liquid film occurred in the downstream area because the metal plate temperature was relatively high when the injection of the liquid jet was stopped. The position at which nucleate boiling can be observed moved subtly upstream owing to the temperature increase of the metal plate surface, and the residual liquid film was fully consumed. The boiling phenomenon of a residual fuel liquid film was also observed during the pulse-firing mode in a quartz chamber [11]. The process of residual liquid film consumption with nucleate boiling described above was successfully captured in the results of the surface heat flux distribution estimated by solving the inverse heat conduction problem.

Figure 6 presents the cooling processes at the beginning of the 2nd and 3rd periods. The white dashed lines indicate the wetting front position at the end of the previous ON time. During the 2nd period, the liquid film rapidly expanded downstream, and at t = 1.1 s, it reached the wetting front position at the end of the 1st ON time, because the temperature of the metal plate surface did not rise to the initial state of the cooling test during the 1st OFF time (Fig. 6). When comparing the 2nd and 3rd periods, we observed that the liquid film expanded farther downstream in the 3rd period (0.1 s after the start of the 3rd injection), because the surface temperature at t = 2.0 s was lower than that at t = 1.0 s. The surface heat fluxes immediately after the start of 2nd and 3rd injections exhibited higher values owing to the rapid propagation of the liquid film, as shown at t = 1.05 and 2.05 s in Fig. 6. Subsequently, the value of the surface heat flux decreased, particularly in the region from near the impingement point to the middle of the liquid film, because the surface temperature decreased because of the rapid film propagation, leading to a decrease in the temperature difference between the metal surface and the liquid film. The wetting front rapidly propagated and reached farther downstream with each successive injection because the temperature rise of the metal plate during the OFF time did not exceed the temperature drop during the previous ON time.

For an overview of the liquid film formation and cooling processes during the pulsed cooling test described thus far, the time history of the wetting front position and estimated temperature on the front surface at a certain position (x = 30.3 mm) on the x axis are presented in Fig. 7. The results of the continuous cooling test under the same flow rate (360 mL/min) are indicated by the dashed line in Fig. 7(a). Additionally, in Fig. 7(b), the time history of the position at which the value of the spatial temperature gradient dT_{w}/dx on the x axis attains its maximum value x_{g} is also plotted. The temperature of the metal plate decreased as the number of injections increased and is higher than that in the continuous cooling test under the same flow rate conditions. Regarding the liquid film behavior, the wetting front positions of the 2nd and 3rd periods appeared upstream of its position at the end of the previous injection because of the temperature rise during each OFF time, and eventually propagated farther downstream. Additionally, the position of the wetting front corresponded to the position at which the value of dT_{w}/dx was maximized, regardless of the pulse period, as observed in the quenching process of continuous injection [14].

The results in this subsection demonstrate that the liquid film behavior during both ON and OFF times can be captured by measuring the temperature of the back side of the plate and solving the inverse heat conduction problem.

3.2 Cooling performance of pulsed cooling

To evaluate the characteristics of pulsed cooling with the same liquid volume under the different injection patterns detailed in Table 1, the wetting front position and heat removed by the liquid film are compared in this section.

3.2.1 Evaluation of wetting front behavior

The wetting front behavior is discussed based on the visualization results. Figure 8 presents the wetting front position at the end of each ON time for the aluminum alloy and copper plates. For reference, the results of continuous cooling at t = 1.0, 2.0, and 3.0 s are also indicated by the gray bar in Fig. 8. The error bars exhibit the maximum and minimum values in the five tests. For the 1st period, the wetting front propagated farther downstream as the DC decreased for both metal plates. For the aluminum alloy plate, the position of the wetting front was almost the same under the conditions of 30% DC to 60% DC and decreased with an increase in DC from 72% to continuous cooling for the 2nd and 3rd periods. In contrast, the wetting front formed on the copper plate maintained approximately the same position in the 2nd period for all conditions except for the 30% DC. Eventually, the position under high-DC conditions (i.e., conditions close to continuous injection) reached the same point as that under the 30% DC. This trend was attributed to the differences in the temperature increase during OFF times, which could have affected wetting front propagation in the subsequent ON time because the injection patterns on both metal plates were the same. Therefore, the positions at which the wetting front appeared after the start of 2nd and 3rd injections were analyzed based on the visualization images. Figure 9 presents an example of the visualization results at the end of the 1st ON time and from the start of the 2nd injection, and the distance between the wetting front position at the end of the N^{th} ON time and where it appears in the $(N+1)^{th}$ ON time Δx_{b}. The error bars represent the maximum and minimum values in the five tests. As displayed in Fig. 9(a), the liquid film expands immediately after the start of re-injection, and the wetting front appears upstream of its position at the end of the previous ON time, as described in Section 3.1. The difference between the position of the wetting front at the end of the 1st/2nd ON time and that at the start of the 2nd/3rd ON times (Δx_{b}) for the copper plate was greater than that for the aluminum alloy plate based on the high thermal diffusivity of the copper plate. Additionally, for the copper plate, there was almost no difference between the Δx_{b} values of the 2nd and 3rd periods, whereas the Δx_{b} value of the 3rd period for the aluminum alloy plate significantly decreased compared to that of the 2nd period. Therefore, a longer OFF time affects the wetting front behavior of the copper plate more significantly, leading to the results illustrated in Fig. 9(b). In contrast, the effect of the longer OFF time for the aluminum alloy plate was weak, particularly during the 2nd OFF time, leading to position of the wetting front shifting farther downstream under low-DC conditions.

To better understand the dynamics of the wetting front, the temperature at the wetting front (T_{wf}) in the present cooling system is discussed. Figure 10 exhibits T_{wf} under each condition. In the figure, the minimum film boiling temperatures or Leidenfrost temperatures predicted by Berenson (based on the hydrodynamic theory) [33] and Spiegler (based on the thermodynamic theory) [34] are indicated as dashed and solid lines, respectively. Although Berenson's model (Eq. (2)) was originally applied to the saturated pool film boiling, Umehara [5] found that the temperature at the boundary between the wetted and dry regions during water jet impingement cooling could be organized using Berenson's model. Spiegler [34] predicted the thermodynamic limit of superheat (TLS) based on the Van der Waals equation as Eq (3). The TLS is the maximum temperature at which pure liquid can maintain its liquid phase in a superheated metastable state [35].

$$T_{\mathrm{MFB}} = T_{\mathrm{sat}} + 0.127\frac{\rho_{\mathrm{v}} h_{\mathrm{lv}}}{k_{\mathrm{v}}}\left[\frac{g(\rho_{\mathrm{l}} - \rho_{\mathrm{v}})}{\rho_{\mathrm{l}} + \rho_{\mathrm{v}}}\right]^{\frac{2}{3}}\left[\frac{\sigma}{g(\rho_{\mathrm{l}} - \rho_{\mathrm{v}})}\right]^{\frac{1}{2}}\left[\frac{\mu_{\mathrm{v}}}{g(\rho_{\mathrm{l}} - \rho_{\mathrm{v}})}\right]^{\frac{1}{3}} \tag{2}$$

$$T_{\mathrm{TLS}} = \frac{27}{32}T_{\mathrm{cr}} \tag{3}$$

Figure 10 reveals that T_{wf} under all conditions is lower than the TLS. This means that the temperature at the position of the wetting front in the present cooling system cannot be explained by the thermodynamic theory. The figure also reveals that T_{wf} gradually decreases and takes almost the same value at 80% DC (225 mL/min) and continuous cooling (180 mL/min) as the flow rate of the liquid decreases. Especially, in the copper plate, T_{wf} at lower-DC conditions is close to the temperature predicted by Berenson's model.

Comparing the aluminum alloy and copper plates, T_{wf} in the copper plate is lower than that in the aluminum plate. We considered the effect of thermal properties of the metal plate on T_{wf} as follows. The deflection of the liquid film at the wetting front is likely to be induced by the sudden expansion of the bubbles [36]. The velocity of the vapor flow triggered by the evaporation of the liquid near the wetting front, u_{v}, can be scaled as follows [37]:

$$u_{\mathrm{v}} \sim \frac{q_{\mathrm{s}}}{\rho_{\mathrm{v}} h_{\mathrm{lv}}} \tag{4}$$

Then, the force unit per area by the vapor flow, P_{v}, is scaled as follows:

$$P_{\mathrm{v}} \sim \rho_{\mathrm{v}} u_{\mathrm{v}}^2 \sim \rho_{\mathrm{v}} \left(\frac{q_{\mathrm{s}}}{\rho_{\mathrm{v}} h_{\mathrm{lv}}}\right)^2 \tag{5}$$

Therefore, the force pushing the liquid film outward is related to the heat input from the metal plate to the liquid film. As the same amount of heat input can be delivered from the copper plate at a lower temperature than that from the aluminum alloy plate owing to the high thermal conductivity, lower values of T_{wf} in the copper plate than in the aluminum alloy plate appeared in Fig. 10 under the same flow rate conditions. In other words, the liquid film is deflected from the copper plate more easily (i.e., at the lower temperature condition). Consequently, the effect of the OFF time on the wetting front behavior becomes evident for the copper plate, as displayed in Fig. 9 (b).

3.2.2 Evaluation of amount of heat removed by liquid film

The heat removed from a metal plate by a liquid film is discussed in this subsection, and the performance of pulsed cooling and continuous cooling is evaluated. The rate of heat transfer from the metal plate to the liquid film $\dot{Q}$ is calculated using Eq. (6).

$$\dot{Q} = \int_{A_{\mathrm{wet}}} q_{\mathrm{s}} dA_{\mathrm{wet}} \quad A_{\mathrm{wet}} : \text{area where } q_{\mathrm{s}} \geq q_{\mathrm{th}} \tag{6}$$

The wetted area A_{wet} was defined as the area in which the local surface heat flux q_{s} was greater than or equal to the threshold value q_{th}, because the value of A_{wet} was overestimated if the wetted area was simply defined as the area with a positive value of q_{s} (Fig. 5). The value of q_{th} was derived from that of q_{s} during a non-cooling (only heating) test, and q_{th} = 0.2 and 0.4 MW/m^2 for the aluminum alloy and copper plates, respectively. Figure 11 presents the calculation results for $\dot{Q}$ and A_{wet} for the conditions of 30%, 50%, and 80% DCs and continuous cooling. For the 1$^{\mathrm{st}}$ period, the heat was transferred faster under the lower-DC conditions based on the higher flow rate of the liquid. The slope $d\dot{Q}/dt$ gradually decreased because the velocity of the wetting front and value of the maximum heat flux achieved in the nucleate boiling region decreased as the wetting front shifted farther downstream [14, 16, 17]. In particular, in the continuous cooling of the aluminum alloy plate, $\dot{Q}$ remained almost constant after approximately t = 0.6 s, although the wetted area gradually expanded. In contrast, $\dot{Q}$ for the copper plate continued to increase over time. There are two possible reasons for the trend of $\dot{Q}$ observed for the aluminum alloy plate. First, the effect of the wetted area expansion competed with that of the decrease in the surface heat flux within the nucleate boiling region. Second, the single-phase forced convection region gradually became dominant in the wetted area, leading to a small temperature change over time. The temperature of the aluminum alloy plate decreased more easily because its thermal inertia is lower than that of copper. Therefore, the ratio of the single-phase forced convection area to the total wetted area was greater for the aluminum alloy plate, leading to the observed trend of $\dot{Q}$. Immediately after the start of the 2nd injection, $\dot{Q}$ increased faster than in the 1st period and exhibited a sharp spike, because the liquid film expanded downstream over a short period (Fig. 6). Subsequently, $\dot{Q}$ for the aluminum alloy plate remained constant or decreased, whereas that for the copper plate increased gently. The trend in $\dot{Q}$ for the 3rd period was not significantly different from that for the 2nd period.

To evaluate and compare the heat transfer characteristics in each period, the amount of heat removed by the liquid film during the Nth pulse period $Q_{N_{\mathrm{th}}}$ was calculated by integrating $\dot{Q}$ in the time dimension as follows:

$$Q_{N_{\mathrm{th}}} = \int_{(N-1)\cdot\tau_{\mathrm{p}}}^{N\cdot\tau_{\mathrm{p}}} \dot{Q}\,dt. \tag{7}$$

Figure 12 presents the calculated results for $Q_{N_{\mathrm{th}}}$. The error bars show the maximum and minimum values in the five tests. The arrows in each color, which correspond to the colors in the legends, represent the value of $Q_{N_{\mathrm{th}}}$ for the continuous cooling test calculated from Eq. (7) by setting the Nth period as $t = (N\text{-}1)\cdot\tau_{\mathrm{p}} - N\cdot\tau_{\mathrm{p}}$. $Q_{1_{\mathrm{st}}}$ increased with an increase in the DC for both metal plates, even though $\dot{Q}$ was higher and the wetted area expanded farther under a lower DC (i.e., higher flow rate). This trend suggests that a longer injection time with a lower flow rate is more effective for cooling with the same usage of liquid when the surface temperature is high and boiling heat transfer is dominant. In the 2nd and 3rd periods for the aluminum alloy, the same trend appeared in the range of 30% DC–50% DC, whereas $Q_{2_{\mathrm{nd}}}$ and $Q_{3_{\mathrm{rd}}}$ decreased with an increase in the DC from 60%. Additionally, the amount of heat removed did not change significantly from the 2nd to 3rd periods for 72% DC−90% DC and continuous cooling, because $\dot{Q}$ was nearly constant under high-DC conditions (Fig. 11). This suggests that a shorter injection time with a higher flow rate favors the removal of heat when the surface temperature is low, and the single-phase forced convection region occupies the wetted area. In contrast, $Q_{2_{\mathrm{nd}}}$ and $Q_{3_{\mathrm{rd}}}$ for the copper plate increased with an increase in the DC, similar to the result in the 1st period. There are two possible reasons for this. First, boiling heat transfer was dominant in each period based on the high thermal inertia of copper. Second, wetting front propagation at a high DC was suppressed because of the high thermal diffusivity of the copper plate (Figs. 8 and 9). To evaluate the difficulty of temperature change of the metal plate, the minimum value of the temperature difference $\Delta T_{\mathrm{min}}(t)$ is introduced as follows:

$$\Delta T_{\mathrm{min}}(t) = \min[T_{\mathrm{s}}(x, y, t) - T_{\mathrm{s}}(x, y, 0)] \tag{8}$$

$T_{\mathrm{s}}(x, y, t) - T_{\mathrm{s}}(x, y, 0)$ has negative values in this study because the metal plate was cooled from the initial state. Its minimum value reflects the maximum temperature drop, and therefore, $\Delta T_{\mathrm{min}}(t)$ indicates the difficulty in changing the temperature. Figure 13 presents the time history of ΔT_{min}. As discussed above, the copper plate was more difficult to cool than the aluminum alloy plate at any DC due to its higher thermal inertia. Figure 14 presents the contribution of heat removal per degree of wall superheat ΔT_{sup} to the total amount of heat removed during each period. The $dQ_{N_{\mathrm{th}}}/Q_{N_{\mathrm{th}}}$ value for continuous cooling was calculated as in Fig. 12. Under lower-DC conditions (30% DC and 50% DC in Fig. 14), for the aluminum alloy plate, the peak of the removed heat for each pulse period appeared in nearly the same range of ΔT_{sup}, because the temperature increased during each OFF time. However, under higher-DC conditions (80% DC and continuous cooling in Fig. 14), the peak shifted to a lower ΔT_{sup}, indicating that the dominant mode of heat transfer changed from boiling to single-phase forced convection. For the copper plate, the heat was transferred in a narrower range of ΔT_{sup} compared to that for the aluminum alloy plate. Additionally, the peak appeared at a higher degree of wall superheat due to the high thermal inertia (Fig. 13), although the peak gradually shifted under higher-DC conditions.

Finally, the performance of pulsed cooling was compared to that of continuous cooling. The total amount of heat removed $Q_{\mathrm{t}}(= \sum Q_{N_{th}})$ was calculated, and the nondimensional removed heat Q^*

was calculated using Eq. (9) to evaluate cooling performance.

$$Q^* = \frac{Q_{\mathrm{t}_{\mathrm{pulse}}}}{Q_{\mathrm{t}_{\mathrm{continuous}}}} \tag{9}$$

The calculated results for Q^* are presented in Fig. 15. For the aluminum alloy plate, Q^* was greater than unity for each DC condition, indicating that more heat was removed in the pulsed cooling tests. Additionally, Q^* exhibited a peak in the range of 50% DC to 60% DC because $Q_{2_{\mathrm{nd}}}$ and $Q_{3_{\mathrm{rd}}}$ exhibited peaks in that range. As illustrated in Figs. 12 and 14, we assume that a longer injection time with a lower flow rate is more favorable for removing heat when boiling heat transfer is dominant, and vice versa. Therefore, we concluded that the balancing of the ON/OFF time produces a scenario in which boiling and single-phase forced convection heat transfer compete for the amount of heat removed, resulting in a peak of Q^* for the aluminum alloy plate. In contrast, Q^* monotonously decreased with a decrease in the DC for the copper plate because boiling heat transfer was dominant for heat removal due to the higher thermal inertia, which suppressed wetting front propagation owing to the higher thermal diffusivity.

4. Conclusions

Cooling tests on superheated metal plates under the intermittent injection of liquid jets were performed to enrich the understanding of liquid film behavior and heat transfer characteristics during pulsed cooling processes. The liquid film behavior and metal temperature were simultaneously measured using a high-speed camera and infrared camera, respectively. In the pulsed cooling tests, the flow rate and DC were varied under the same injection quantity to enhance the cooling performance with the same usage of coolant. A continuous cooling test with a time-averaged flow rate of pulsed cooling was also conducted. Two types of metal plates (aluminum alloy and copper) were used to investigate the effects of their thermal properties on the cooling performance.

The wetting front of the liquid film gradually propagated downstream after the start of cooling. When the injection was stopped, the residual liquid film was consumed by nucleate boiling. Immediately after re-injection, the liquid film rapidly expanded because the temperature increase of the metal plate during the OFF time did not exceed the temperature reduction during the previous ON time, at least not for the parameters considered in this study. Therefore, the metal plates were cooled with each cycle of injection. Unsteady liquid film behavior and heat transfer characteristics can be successfully captured by measuring the opposite-side temperature of the surface cooled by a liquid film and solving the inverse heat conduction problem.

The wetting front position and amount of heat removed by the liquid film were evaluated under various conditions. For the 1st pulse, where boiling was the dominant mode for cooling, a longer injection time was more effective for removing heat, although the wetting front was shorter with a higher DC. In subsequent pulses, the amount of heat removed by the liquid film peaked at 50% DC and decreased with the increase in the DC from 60% for the aluminum alloy. This may have been caused by the cooling mode shifting from boiling to single-phase forced convection, particularly under high-DC (60% DC–90% DC) conditions. In contrast, the same trend observed in the 1st pulse continued for the copper plate. There are two possible explanations for this trend. First, boiling could have remained the dominant mode of heat transfer during subsequent pulses because the temperature of the copper plate did not easily change due to its high thermal inertia. Second, wetting front propagation was suppressed more with a longer OFF time owing to the high thermal diffusivity of the plate. Finally, the total amount of heat removed by the liquid film during the pulsed cooling was compared to that during the continuous cooling. For the aluminum alloy, the cooling performance was improved by a maximum of 13% with pulsed cooling compared to that with continuous cooling. In contrast, for the copper plate, the cooling performance of pulsed cooling was inferior to that of continuous cooling, with a maximum reduction of 20%.

References

[1] C. F. Gomez, C. W. M. van der Geld, J. G. M. Kuerten, M. Bsibsi, and B. P. M. van Esch, 'Film boiling in quench cooling with high-temperature jets', International Journal of Heat and Mass Transfer, vol. 164, Article 120578, 2021.

[2] S. G. Lee, M. Kaviany, C. J. Kim, and J. Lee, 'Quasi-steady front in quench subcooled-jet impingement boiling: Experiment and analysis', International Journal of Heat and Mass Transfer, vol. 113, pp. 622–634, 2017.

[3] A. V. S. Oliveira et al., 'Experimental study of the heat transfer of single-jet impingement cooling onto a large heated plate near industrial conditions', International Journal of Heat and Mass Transfer, vol. 184, Article 121998, 2022.

[4] D. H. Wolff, F. P. Incropera, and R. Viskanta, 'Local jet impingement boiling heat transfer', International Journal of Heat and Mass Transfer, vol. 39, issue. 7, pp. 1395–1406, 1996.

[5] Y. Umehara, K. Yamagata, and T. Okawa, 'Spatial distribution of heat transfer coefficient in the vicinity of wetting front during falling liquid film cooling of a vertical hot wall', International Journal of Heat and Mass Transfer, vol. 185, Article 122422, 2022.

[6] G. Fujii, Y. Daimon, K. Furukawa, C. Inoue, D. Shiraiwa, and N. Tanaka, 'Visualization of Coolant Liquid Film Dynamics in Hypergolic Bipropellant Thruster', Journal of Propulsion and Power, vol. 38, no. 2, pp. 267–273, 2022.

[7] L. jun Yang, P. hui Li, and Q. fei Fu, 'Liquid sheet formed by a Newtonian jet obliquely impinging on pro/hydrophobic surfaces', International Journal of Multiphase Flow, vol. 125, Article 103192, 2020.

[8] N. Sako, J. Hayashi, Y. Daimon, H. Tani, and H. Kawanabe, 'Experimental analysis of the spreading of a liquid film on a bipropellant thruster chamber wall', Journal of Thermal Science and Technology, vol. 16, Issue 1, pages JTST0008, 2021.

[9] J. Hayashi et al., 'Multilayer reaction zones of a counterflow flame of gaseous Nitrogen Tetroxide and a liquid Monomethylhydrazine pool', Combustion and Flame, vol. 201, pp. 244–251, 2019.

[10] H. Tani, Y. Daimon, M. Sasaki, and Y. Matsuura, ‘Atomization and hypergolic reactions of impinging streams of monomethylhydrazine and dinitrogen tetroxide’, Combustion and Flame, vol. 185, pp. 142–151, 2017.

[11] G. Fujii, Y. Daimon, C. Inoue, D. Shiraiwa, N. Tanaka, and K. Furukawa, ‘Visualization of pulse firing mode in hypergolic bipropellant thruster’, Journal of Propulsion and Power, vol. 36, no. 5, pp. 671–684, 2020.

[12] Y. Daimon, H. Negishi, H. Tani, Y. Matsuura, S. Iihara, and S. Takata, ‘Flow field and heat transfer analysis in a MON/MMH bipropellant rocket engine’, International Journal of Energetic Materials and Chemical Propulsion, vol. 16, no. 3, pp. 263–280, 2017.

[13] S. Takata, Y. Daimon, K. Sugimori, N. Matsuda, and Y. Tashiro, ‘Design verification results of japanese 120N Bi-propellant thrusters (HBT-1) based on its first flight in HTV3’, 49th AIAA/ASME/SAE/ASEE Joint Propulsion Conference, AIAA-2013-3754, 2013.

[14] N. Sako, K. Noda, J. Hayashi, Y. Daimon, and H. Kawanabe, ‘Quenching of a heated wall with spatial temperature gradient using a liquid film through oblique jet impingement’, International Journal of Heat and Mass Transfer, vol. 192, Article 122925, 2022.

[15] M. Monde, ‘Heat Transfer Characteristics during Quench of High Temperature Solid’, Journal of Thermal Science and Technology, vol. 3, no. 2, pp. 292–308, 2008.

[16] N. Karwa, T. Gambaryan-Roisman, P. Stephan, and C. Tropea, ‘Experimental investigation of circular free-surface jet impingement quenching: Transient hydrodynamics and heat transfer’, Experimental Thermal and Fluid Science, vol. 35, issue 7, pp. 1435–1443, 2011.

[17] A. K. Mozumder, M. Monde, P. L. Woodfield, and M. A. Islam, ‘Maximum heat flux in relation to quenching of a high temperature surface with liquid jet impingement’, International Journal of Heat and Mass Transfer, vol. 49, issues 17–18, pp. 2877–2888, 2006.

[18] C. Agrawal, R. Kumar, A. Gupta, and B. Chatterjee, ‘Rewetting and maximum surface heat flux during quenching of hot surface by round water jet impingement’, International Journal of Heat and Mass Transfer, vol. 55, issues 17–18, pp. 4772–4782, 2012.

[19] B. Wang, D. Lin, Q. Xie, Z. Wang, and G. Wang, 'Heat transfer characteristics during jet impingement on a high-temperature plate surface', Applied Thermal Engineering, vol. 100, pp. 902–910, 2016.

[20] D. J. Butterfield, B. D. Iverson, D. Maynes, and J. Crockett, 'Transient heat transfer of impinging jets on superheated wetting and non-wetting surfaces', International Journal of Heat and Mass Transfer, vol. 175, Article 121056, 2021.

[21] A. H. Nobari, V. Prodanovic, and M. Militzer, 'Heat transfer of a stationary steel plate during water jet impingement cooling', International Journal of Heat and Mass Transfer, vol. 101, pp. 1138–1150, 2016.

[22] Y. Liu, H. Nakai, Y. Mitsutake, and M. monde, 'Experimental study on transient boiling heat transfer around wetting front during subcooled jet impingement quenching', Thermal science and engineering, vol. 29, no. 1. pp. 9–17, 2021.

[23] J. Wassenberg, P. Stephan, and T. Gambaryan-Roisman, 'Heat transfer during pulsating liquid jet impingement onto a vertical wall', Heat and Mass Transfer/Waerme- und Stoffuebertragung, vol. 57, issue 4, pp. 617–629, 2021.

[24] S. Abishek and R. Narayanaswamy, 'Low Frequency Pulsating Jet Impingement Boiling and Single Phase Heat Transfer', International Journal of Heat and Mass Transfer, vol. 159, Article 120052, 2020.

[25] Q. Ye, Y. Zhang, and J. Wei, 'A comprehensive review of pulsating flow on heat transfer enhancement', Applied Thermal Engineering, vol. 196, Article 117275, 2021.

[26] R. C. Schindler and L. Schoenman, 'Development of a five-pound thrust bipropellant engine', Journal of Spacecraft and Rockets, vol. 13, no. 7, pp. 435–442, 1976.

[27] N. Tanaka, D. Shiraiwa, T. Kaneko, and K. Furukawa, 'Development of Low-thrust Thruster with World's Highest Performance Contributing to Life Extension of Artificial Satellites', Mitsubishi Heavy Industries Technical Review, vol. 54, no.4, 2017.

[28] S. D. Rosenberg and L. Schoenman, 'New generation of high-performance engines for space

propulsion', Journal of Propulsion and Power, vol. 10, no. 1, pp. 40–46, 1994.

[29] T. Inoue, C. Inoue, G. Fujii, and Y. Daimon, 'Evaporation of Three-Dimensional Wavy Liquid Film Entrained by Turbulent Gas Flow', AIAA Journal, vol. 60, no. 6, pp. 3805–3812, 2022.

[30] C. Liu, C. Tang, H. Mu, and Z. Huang, 'A data fusion approach with high spatiotemporal resolution for wall temperature measurement upon jet impingement', International Journal of Heat and Mass Transfer, vol. 183, Article 122084, 2022.

[31] K. Tsukamoto et al., 'On the onset of quench during spray cooling: The significance of oxide layers', Applied Thermal Engineering, vol. 179, Article 115682, 2020.

[32] N. Sako, J. Hayashi, C. Inoue, H. Kawanabe, and Y. Daimon, 'Boiling induced atomization appeared in the liquid film by wall impinging jet on the superheated wall' Proceedings of International Conference on Liquid Atomization and Spray Systems ICLASS 2021, Paper 287, 2021.

[33] P. J. Berenson, 'Film boiling heat transfer from a horizontal surface', Transactions of the ASME, Journal of Heat Transfer, vol. 83, pp. 351–358, 1961.

[34] P. Spiegler, J. Hopenfeld, M. Silberberg, C. F. Bumpus, and A. Norman, 'Onset of stable film boiling and the foam limit', International Journal of Heat and Mass Transfer, vol. 6, pp. 987–994, 1963.

[35] C. F. Gomez et al., 'The nature of boiling during rewetting of surfaces at temperatures exceeding the thermodynamic limit for water superheat', Journal of Fluid Mechanics, vol. 179, Article A3, 2020.

[36] S. Waldeck, H. Woche, E. Specht, and U. Fritsching, 'Evaluation of heat transfer in quenching processes with impinging liquid jets', International journal of thermal sciences, vol. 134, pp. 160-167, 2018.

[37] J. Breitenbach, J. Kissing, I. V. Roisman, and C. Tropea, 'Characterization of secondary droplets during thermal atomization regime', Experimental Thermal and Fluid Science, vol. 98, pp. 516-522, 2018.

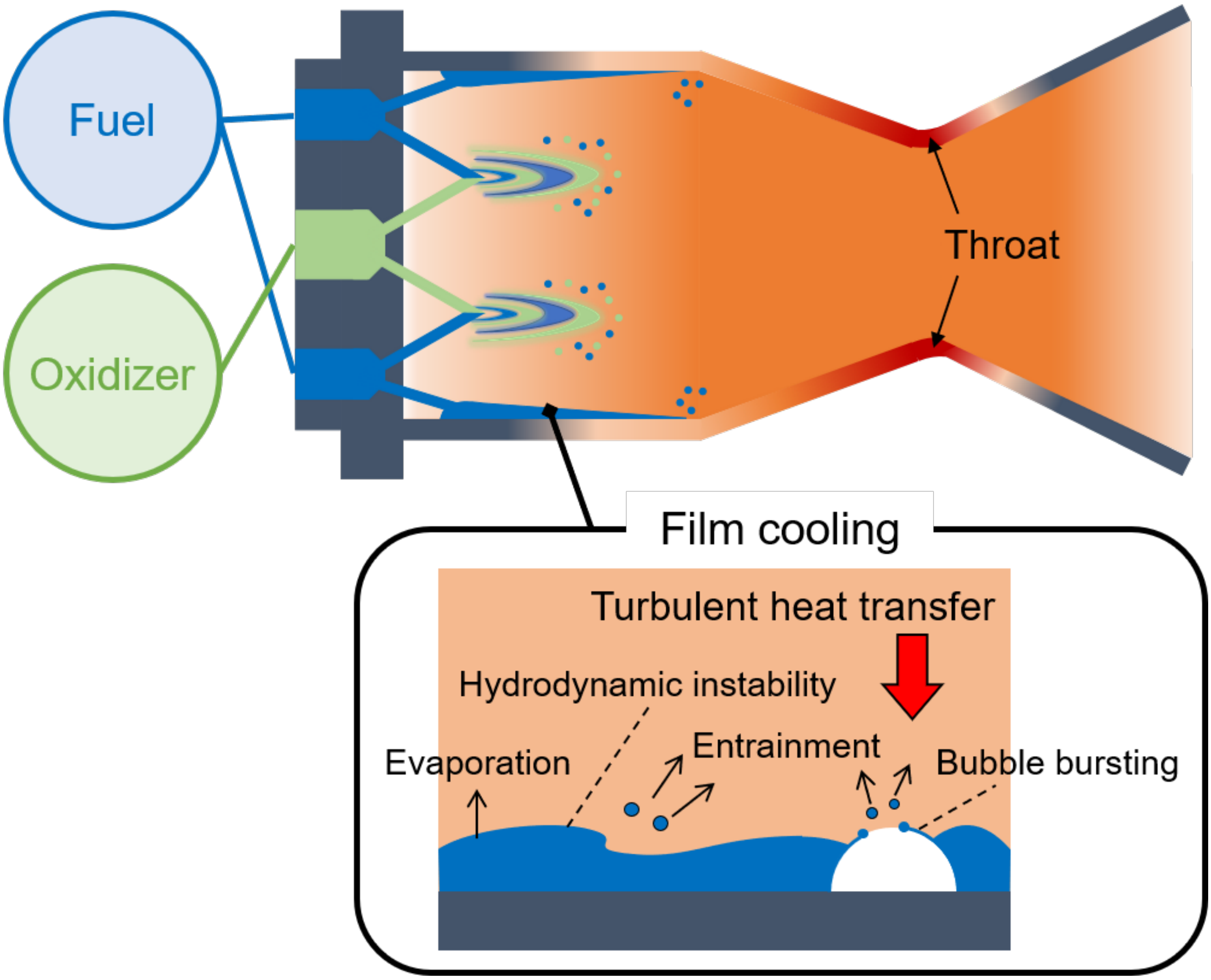

Fig. 1 Schematic of film cooling in the combustion chamber of bipropellant thrusters.

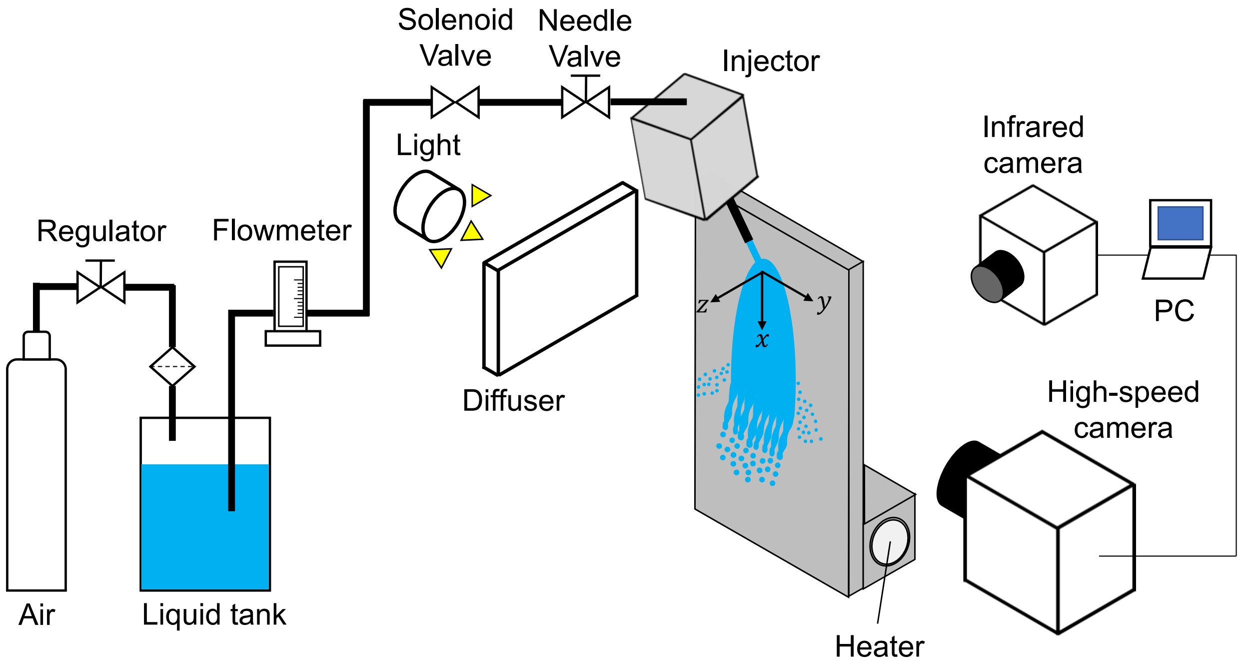

Fig. 2 Schematic of the experimental apparatus.

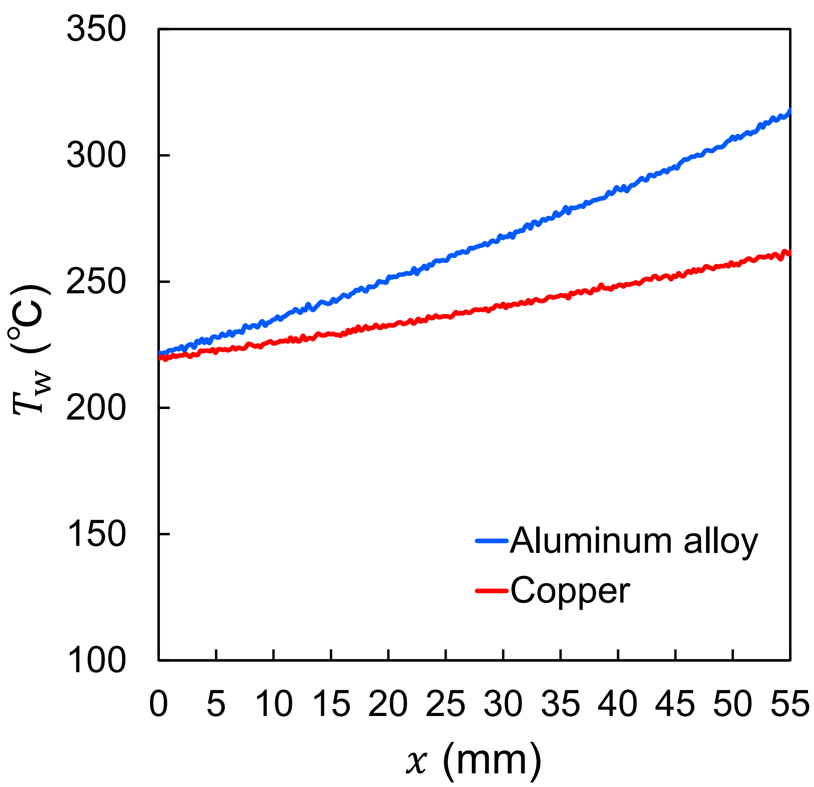

Fig. 3 Initial temperature distribution along the x axis.

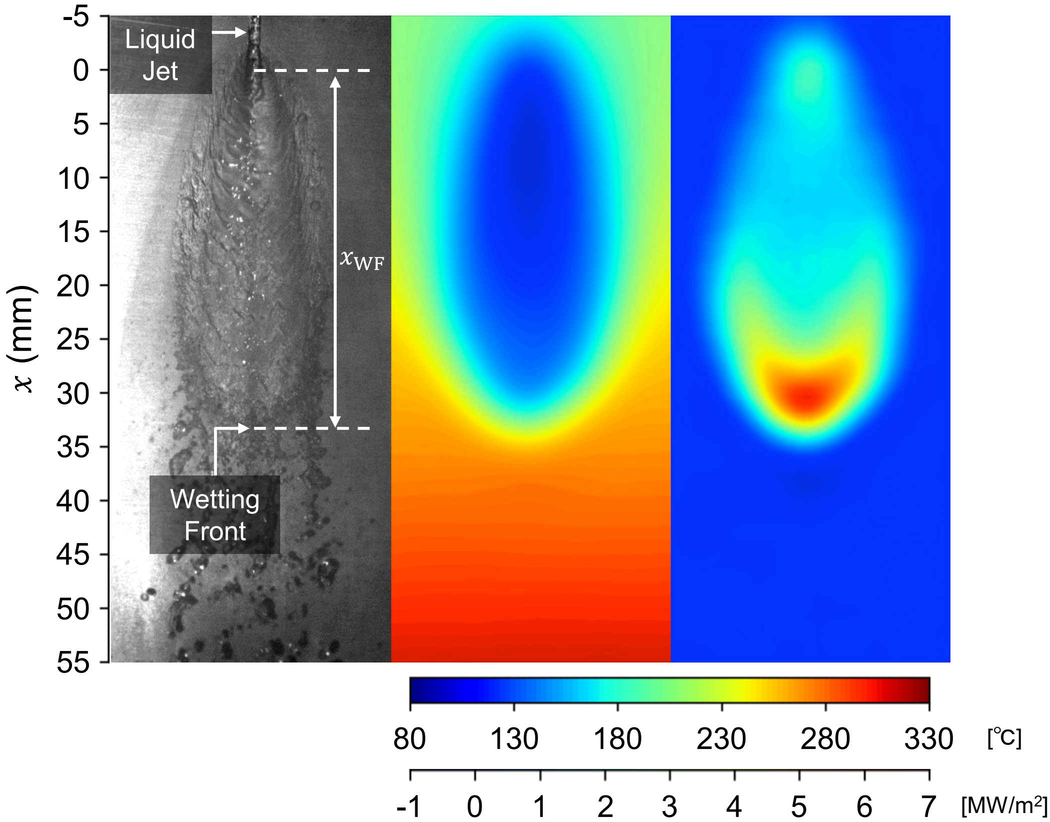

Fig. 4 Liquid film (left), and estimated temperature (middle) and heat flux (right) distribution on the front surface at t = 0.5 s.

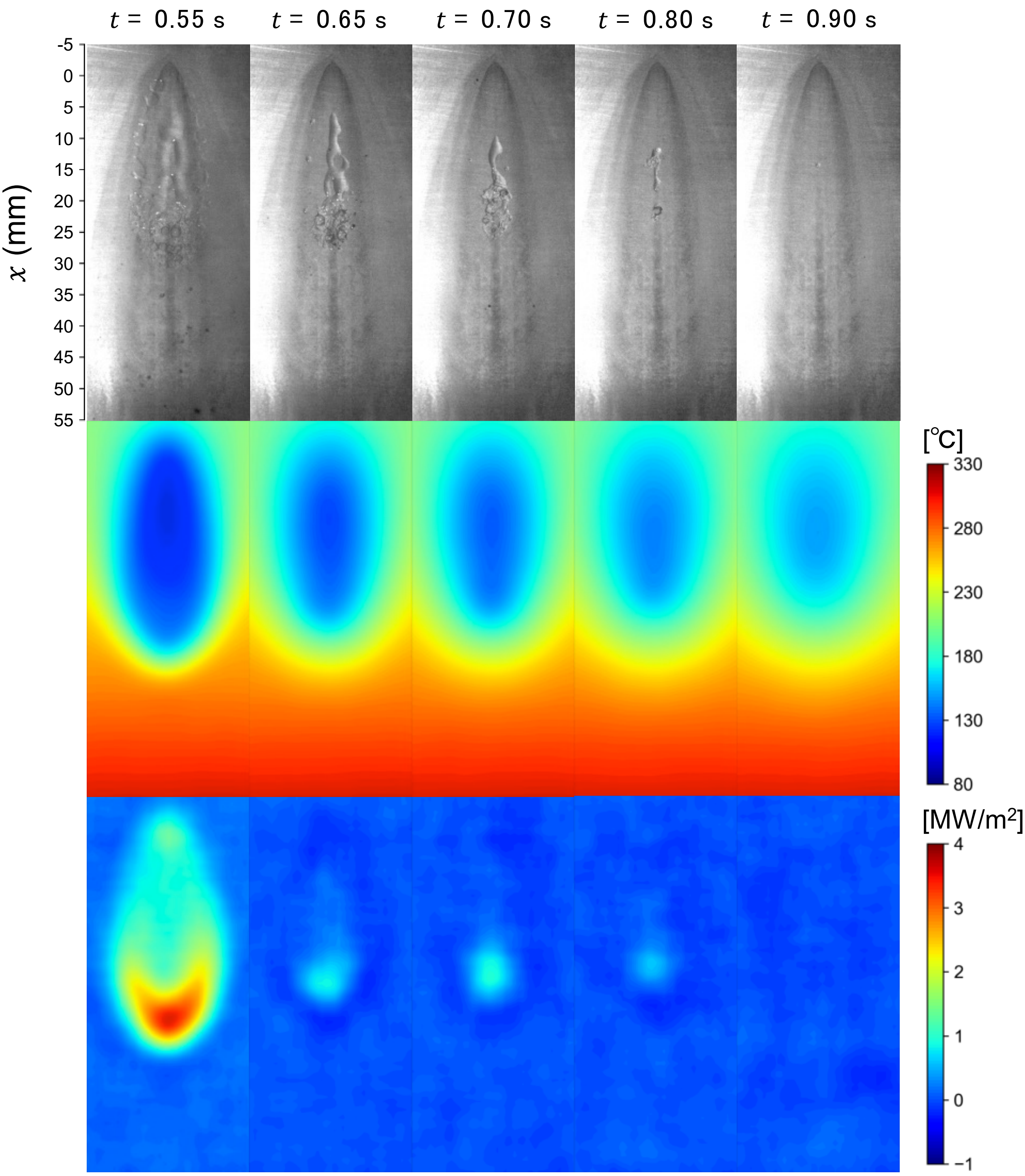

Fig. 5 Evaporation process of liquid film during the 1st OFF time: images (upper), and estimated temperature (middle) and heat flux (bottom) distributions on the front surface.

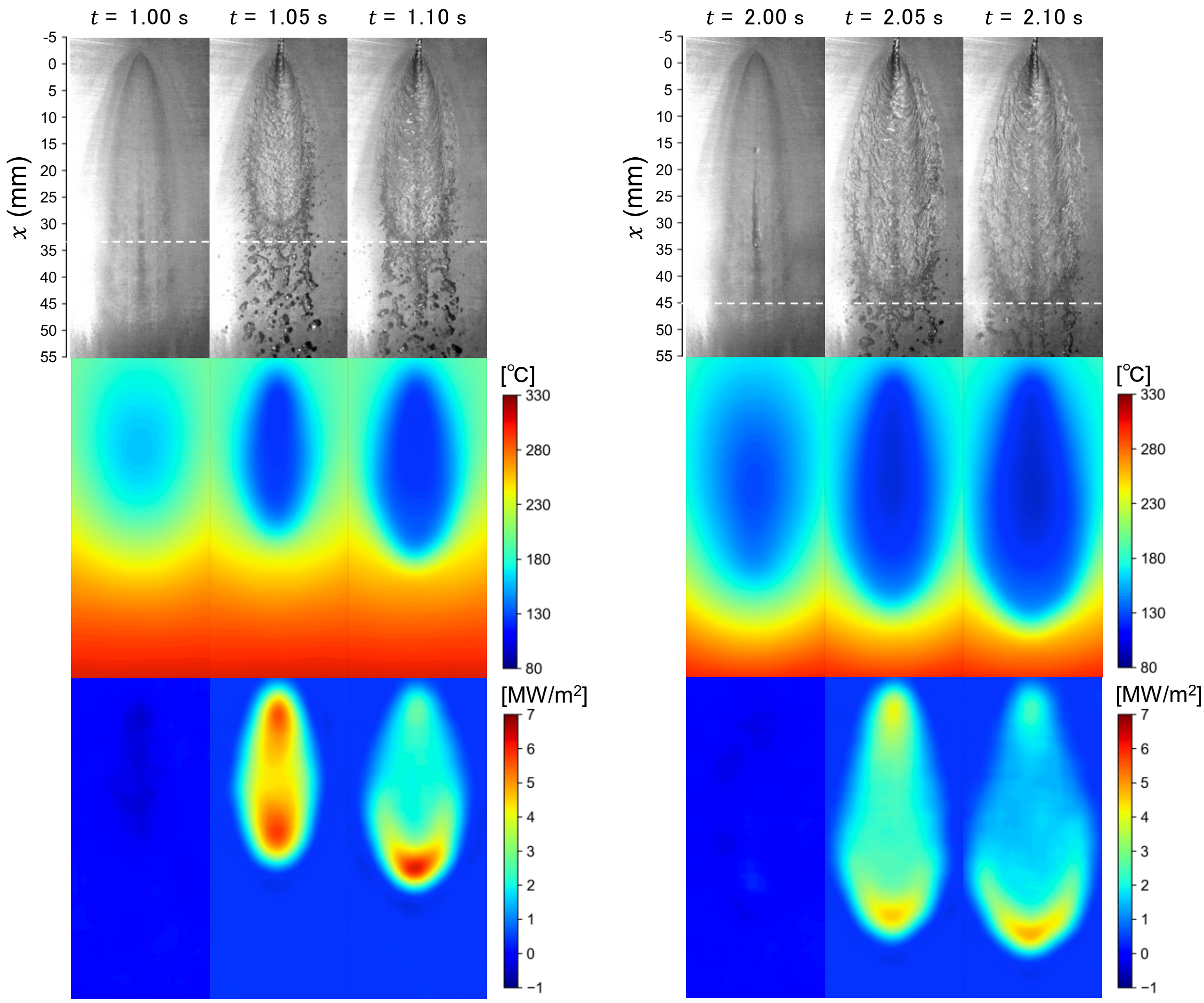

Fig. 6 Propagation of the liquid film during the 2nd (left) and 3rd (right) periods: images (upper), and estimated temperature (middle) and heat flux (bottom) distributions on the front surface. White dashed lines in each image indicate the wetting front position at the end of the previous ON time.

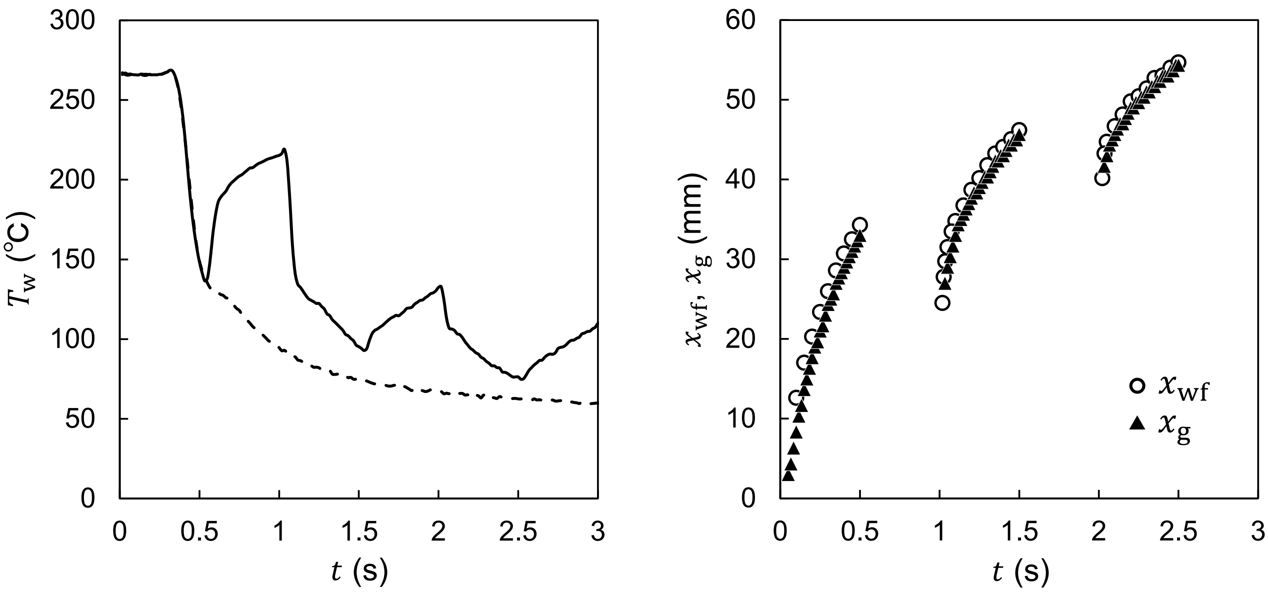

Fig. 7 Time histories of the temperature at x = 30.3 mm on the x axis and positions of x_{wf} and x_g.

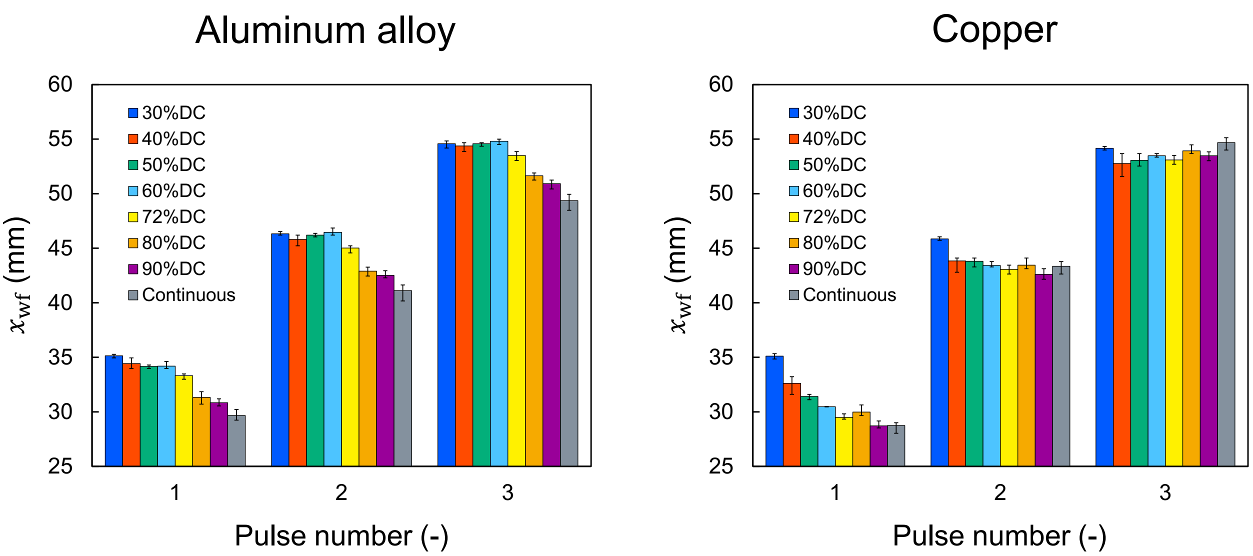

Fig. 8 Wetting front position at end of each ON time; (left) aluminum alloy, (right) copper.

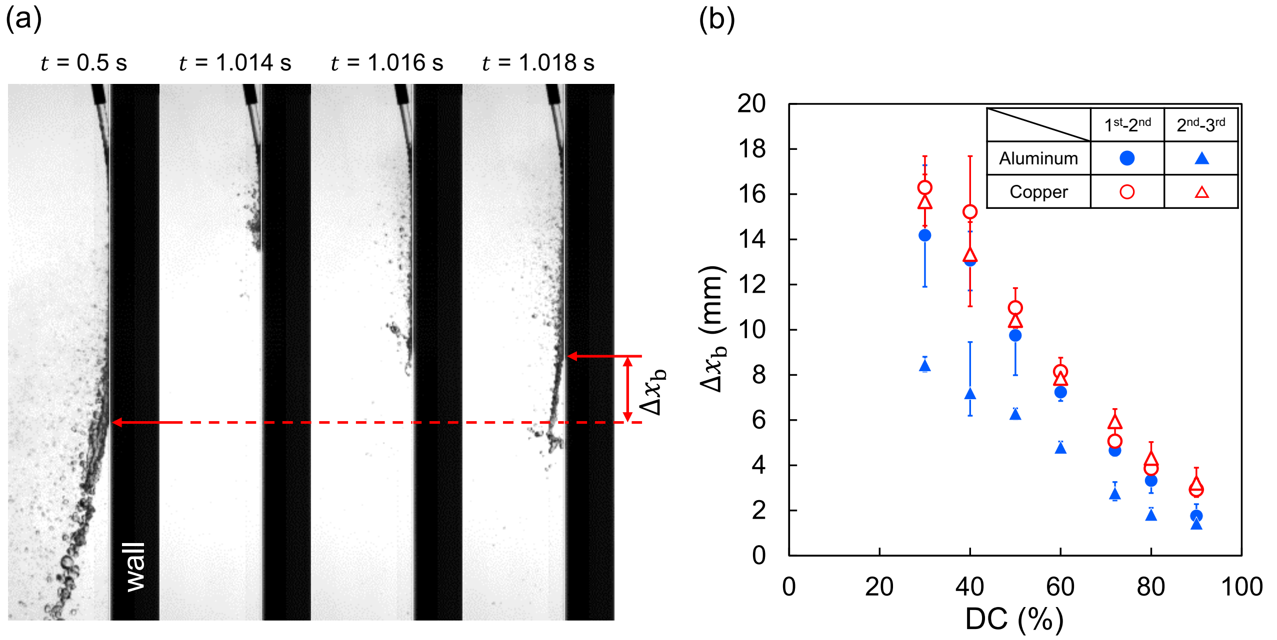

Fig. 9 (a) Side view of the propagation process of liquid films after re-injection, and (b) Δx_{b} values under each condition.

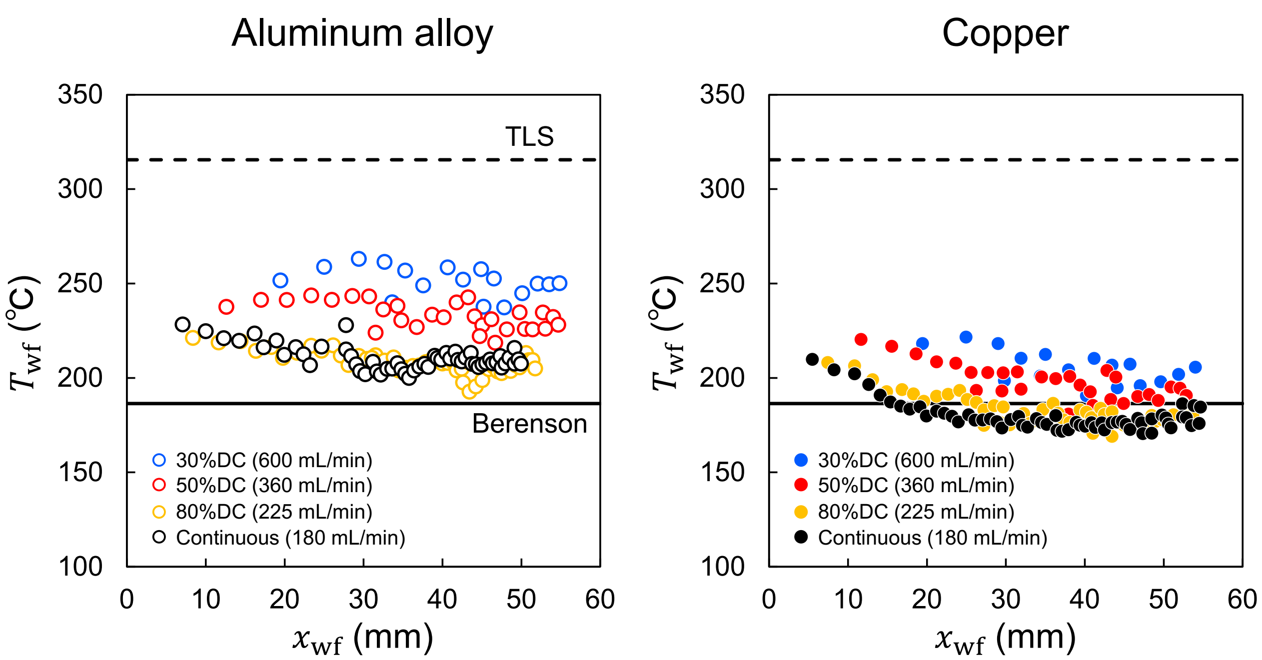

Fig. 10 Temperatures at the wetting front; (left) aluminum alloy, (right) copper.

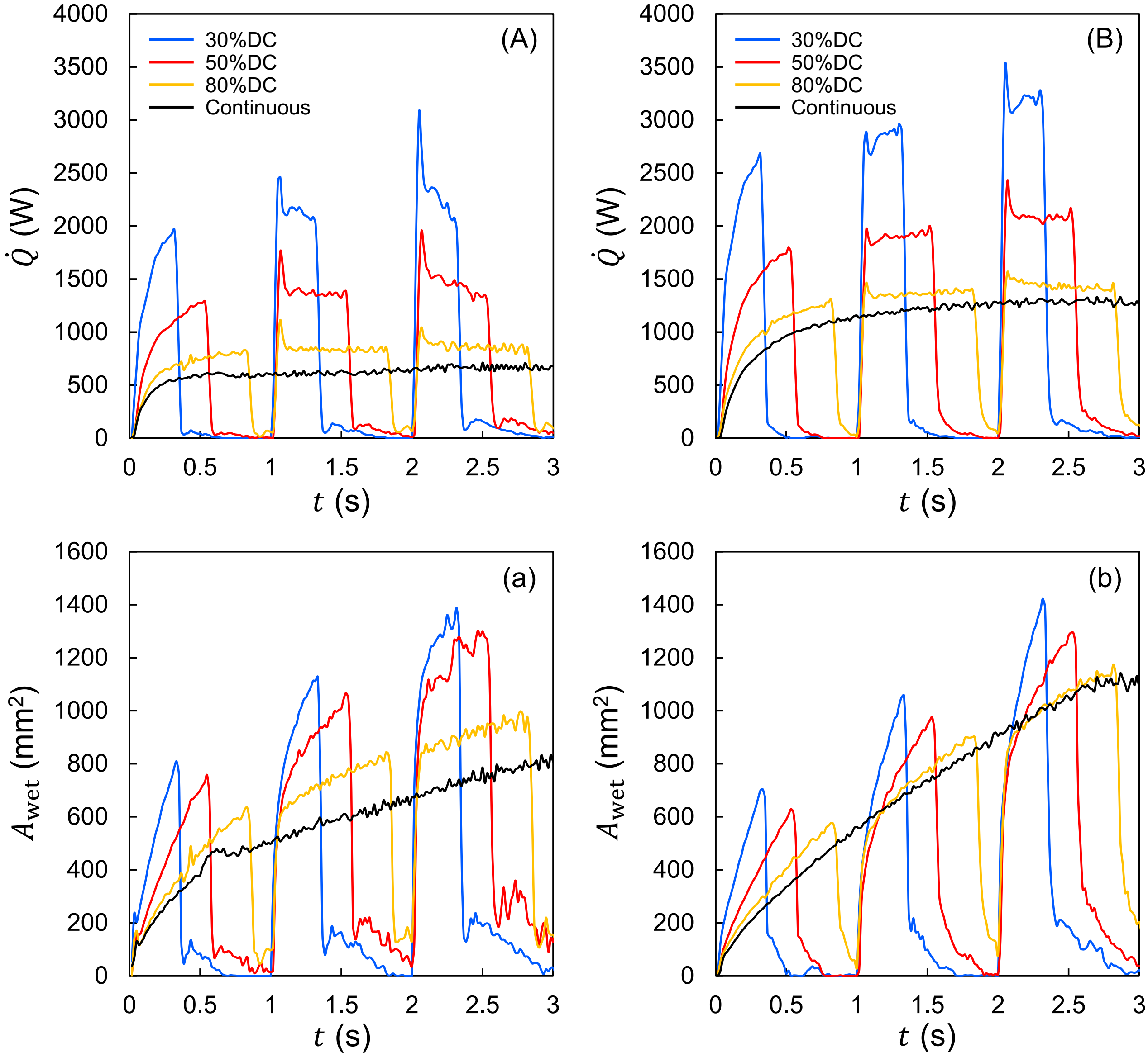

Fig. 11 Time histories of the rate of heat transfer and wetted area: (A, a) aluminum alloy and (B, b) copper.

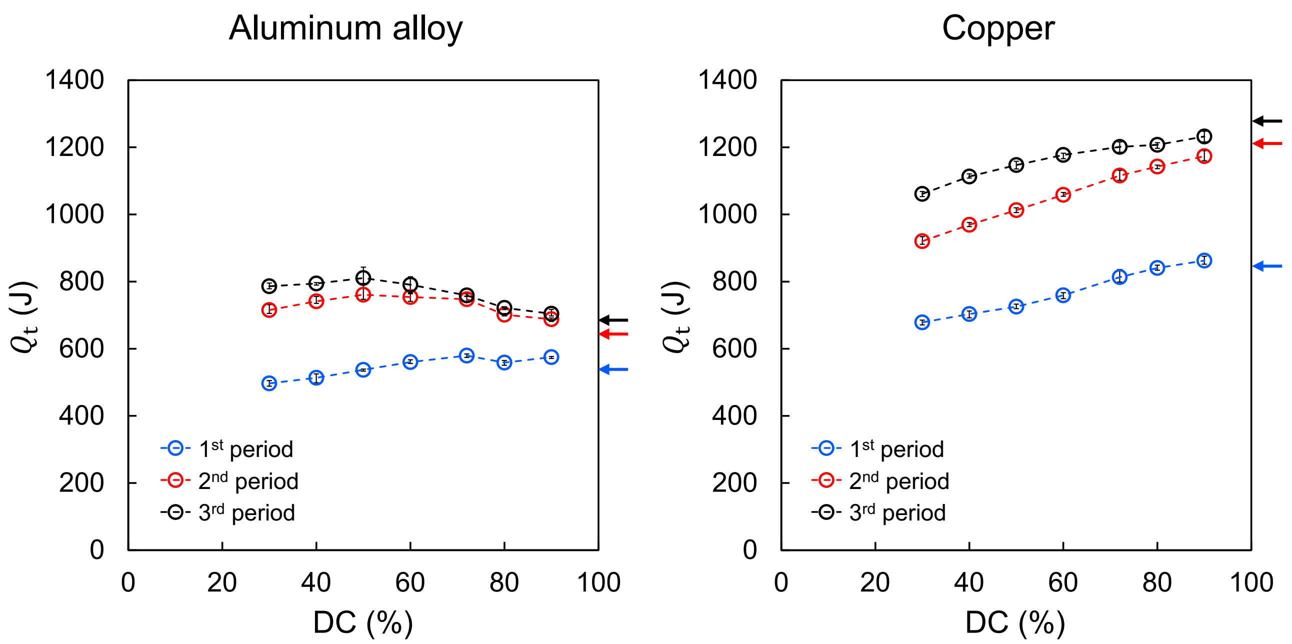

Fig. 12 Amounts of heat removed during each period: (left) aluminum alloy and (right) copper.

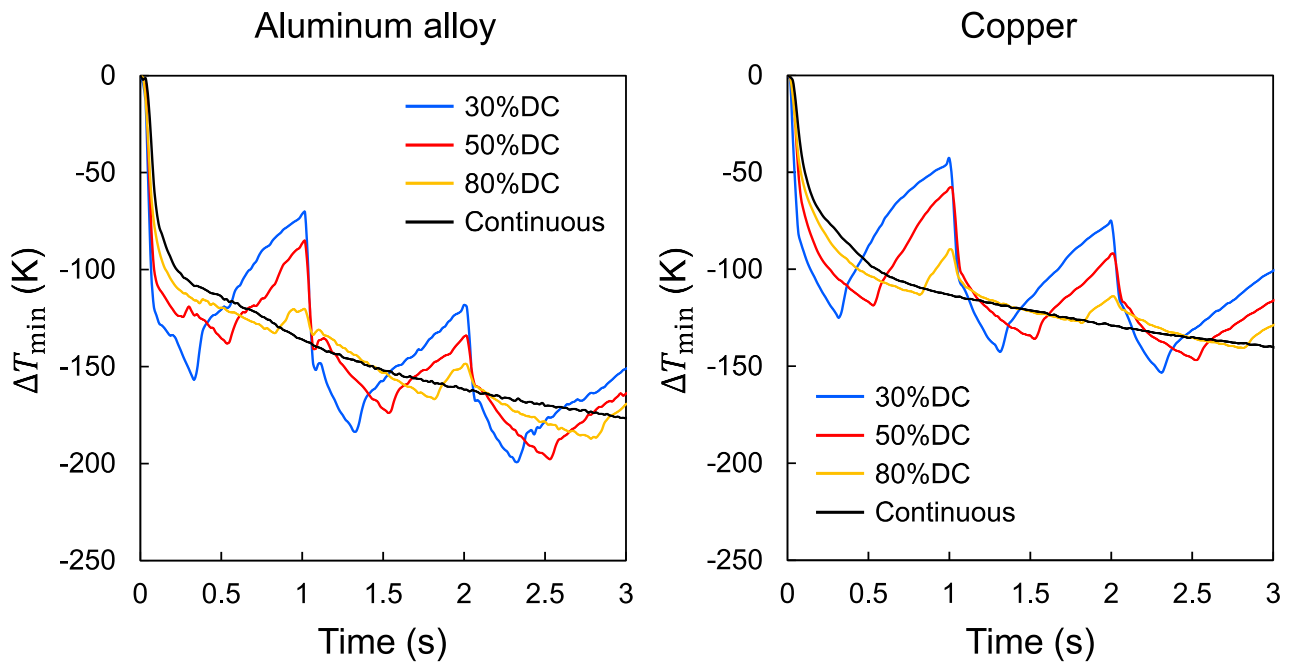

Fig. 13 Time histories of the minimum values of the temperature differences defined in Eq. (8): (left) aluminum alloy and (right) copper.

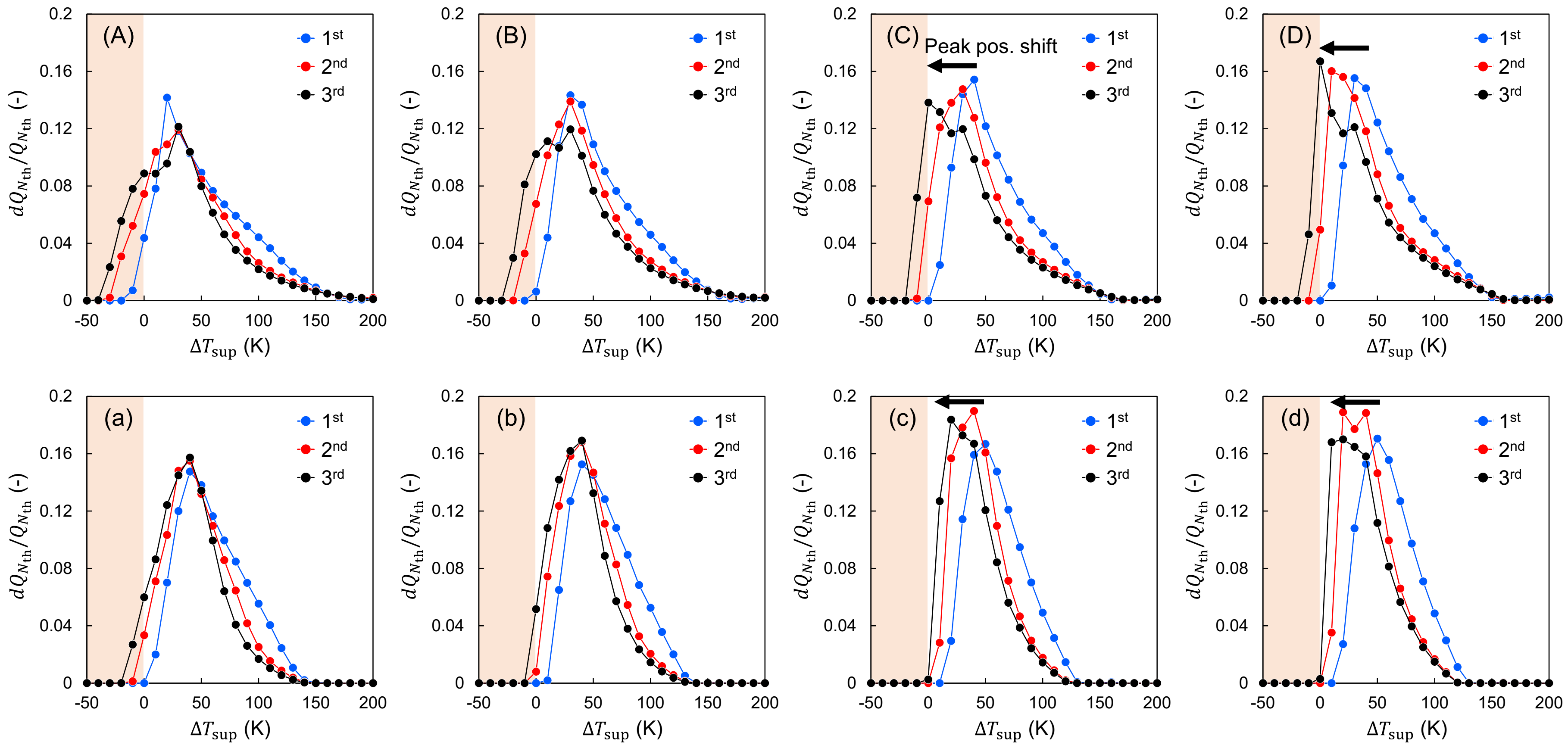

Fig. 14 Contribution of removed heat per degree of wall superheat to the total amount of heat removed during each period. (A, a) 30% DC, (B, b) 50% DC, (C, c) 80% DC, (D, d) continuous injection. Capital letters and small letters represent the results for the aluminum alloy and copper plates, respectively.

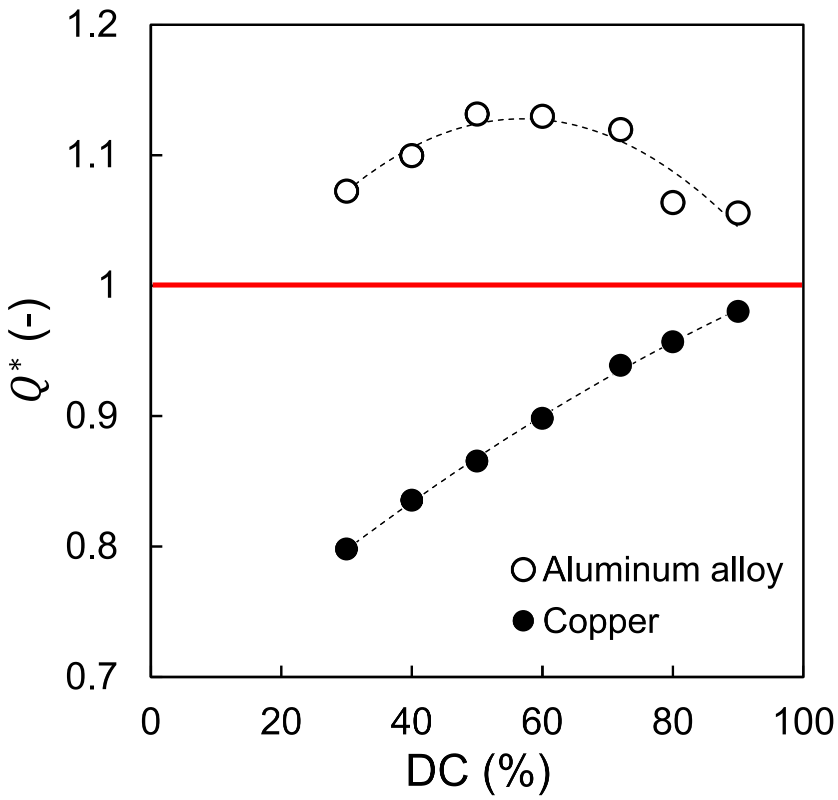

Fig. 15 Nondimensional heat removed by liquid film calculated using Eq. (9).

Table 1 Injection patterns

DC, %	Flow rate, L/min	Jet Reynolds number	Injection time, s
30	600	11500	0.30
40	450	8600	0.40
50	360	6900	0.50
60	300	5800	0.60
72	250	4800	0.72
80	225	4300	0.80
90	200	3800	0.90
100 (continuous)	180	3500	3.00